Monodisperse Gold Nanorods for High-pressure Refractive-index Sensing.

Camino Martín-Sánchez, Guillermo González-Rubio, Paul Mulvaney,
Andrés Guerrero-Martínez, Luis M. Liz-Marzán, and Fernando Rodriguez

Just Accepted

Monodisperse gold nanorods for high-pressure refractive-index sensing

Camino Martín-Sánchez[a] , Guillermo González-Rubio[b,c] , Paul Mulvaney[d] , Andrés Guerrero-Martínez[c] , Luis M. Liz-Marzán[b,e] , Fernando Rodríguez[a,]*

[a] MALTA, DCITIMAC, Facultad de Ciencias, University of Cantabria, Santander, 39005, Spain

[b] CIC biomaGUNE and CIBER-BBN, Paseo de Miramón 182, 20014 Donostia-San Sebastián, Spain

[c] Departamento de Química Física, Universidad Complutense de Madrid, Avenida Complutense s/n, 28040 Madrid, Spain.

[d] ARC Centre of Excellence in Exciton Science, School of Chemistry, University of Melbourne, Victoria, 3010, Australia

[e] Ikerbasque, Basque Foundation for Science, Bilbao 43018, Spain

1

ABSTRACT. The effects of hydrostatic pressure on the surface plasmon resonances (SPR) of aqueous dispersions of monodisperse gold nanorods were determined up to 9 GPa. The ultranarrow longitudinal SPR band of monodisperse nanorods allows us to monitor a gradual redshift with pressure, which shows abrupt jumps at the liquid to ice phase VI and ice phase VII transitions. Despite solidifying at low pressure (about 1 GPa), water displays a regime of quasi-hydrostaticity in said phase VI and VII, up to *ca*. 5 GPa. Above this pressure, non-hydrostatic effects manifest themselves through broadening of the SPR bands, but barely any effect is observed on the position of the SP mode. The variation in the SPR peak wavelength with pressure allowed us to determine the pressure dependence of the refractive index of water. Unlike Brillouin scattering or interferometric techniques, this plasmon spectroscopy based method leads to a more direct determination of the refractive index, which is well described empirically by Murnaghan-type equations in the three explored phases. We report herein the obtained analytical functions providing the pressure dependence of refractive index in the liquid, ice VI and ice VII phases of water.

INTRODUCTION

The application of hydrostatic pressure to nanoscale materials is an efficient method to induce changes in their physico-chemical properties through volume reduction of both the nanoparticles and their surrounding medium. This is due to the ability of nanoscale materials to exhibit size dependent optical, magnetic, electronic, and catalytic properties, which render them promising candidates for applications ranging from biomedicine to electronic displays [1–3]. However, a major challenge has been understanding and eventually predicting changes in nanomaterials properties due to structural changes of either the nanoparticles, the surrounding medium or both. This behavior can be monitored *via* surface plasmon resonances in metal nanoparticles of various shapes (*e.g.* nanospheres and nanorods), due to changes in their aspect ratio (AR) or nanoparticle size, as well as in the refractive index of the surrounding medium. Gold nanorod (AuNR) plasmonics has been recently exploited to investigate the nanoparticle's mechanical properties, through adequate models describing SPR shifts under hydrostatic and non-hydrostatic high-pressure conditions [4]. This new methodology is noteworthy owing to the difficulty in applying well-defined loading forces to nanomaterials, as well as problems related to measuring deformations with suitable accuracy. Although high-pressure measurements have been previously carried out on metal nanoparticles [5, 6], only a few studies have been able to properly describe the observed changes in terms of pressure-induced structural variations, because of the severe non-hydrostatic conditions. We present herein for the first time, the application of spectroscopic measurements of the SPR of aqueous solutions of monodisperse AuNRs under hydrostatic loading, to determine the pressure-dependence of the refractive index of water, both in the liquid state and in ice phases VI and VII. AuNRs with optical monodispersity were obtained by controlled irradiation with femtosecond laser pulses, following a previously established procedure [7]. This

method yields the highest reported optical quality for AuNRs, related to a minimum dispersion in aspect ratio, which in the present work corresponds to an average AR of 3.4 and a standard deviation of 0.2. This highly narrow size distribution is crucial for accurate measurement of pressure-induced deviations of the longitudinal surface plasmon resonance (LSPR) peak, extinction cross-section or extinction bandwidth. Measurements of these three parameters as a function of pressure, in the 0-9 GPa range allow us to extract information on the refractive index $n(P)$ of water, as well as on AuNR aggregation in the solid phases. We demonstrate that LSPR spectral shifts of AuNR aqueous solutions can be used to infer the value of $n(P)$ for water in the liquid state, as well as in the ice phases VI and VII. The obtained results compared well to data obtained by other techniques: on one hand Brillouin spectroscopy and sound velocity [8], and on the other hand interferometry and reflectivity techniques [9–11]. Interestingly, this plasmonics based method for the determination of $n(P)$ has the advantage of providing a more direct measure of the refractive index, whereas methods based on Brillouin spectroscopy and interferometric measurements depend on the accurate measurement of two independent variables – the Brillouin peak shift and sound velocity, and interference pattern and interlayer distance, respectively–, our surface plasmon-based method depends on the solvent refractive index and the bulk modulus of gold in the nanoparticle, but the latter accounts for less than 10% of the total contribution to the SPR pressure shift, thus providing an attractive alternative approach to determine $n(P)$.

RESULTS

Figure 1 presents a representative transmission electron microscopy (TEM) image and corresponding histogram of the employed AuNRs, as well as experimental and calculated extinction spectra. The AuNRs can be approximated as spherically capped cylinders with a diameter of 13.4 nm, and end-cap geometry – defined as the spherical-cap height-to-diameter ratio

– of 0.4. The AuNRs are highly monodisperse, with an aspect-ratio distribution centered at 3.4 and standard deviation of 0.2. The optical spectrum shows the characteristic band structure associated with the transversal SPR located at 510 nm (weak band) and the longitudinal SPR at 740 nm (strong band), in accordance with the measured aspect ratio of 3.4 and correlations between LSPR and aspect ratio in AuNR aqueous dispersions established elsewhere [12]. The extinction spectra were simulated using a modified Mie-Gans model to account for AuNR distribution and geometry (end-cap, roughness and dimensions; retardation effects) [13,14]. The model suitability is illustrated though the simulated spectrum shown in Figure 1. It should be noted that the AuNR response used in this simulation coincides with that calculated by R. Yu *et al*. for a rod-shaped nanoparticle (see Fig. S1 in Supporting Information (SI)) [15]. Neither extinction background nor gold-interband refractive-index effects at the nanoscale were considered in the simulation. All those effects mainly influence the spectral region below 550 nm and probably account for the observed discrepancies in the transversal SPR band. However, this correction does not affect the LSPR position and the band width.
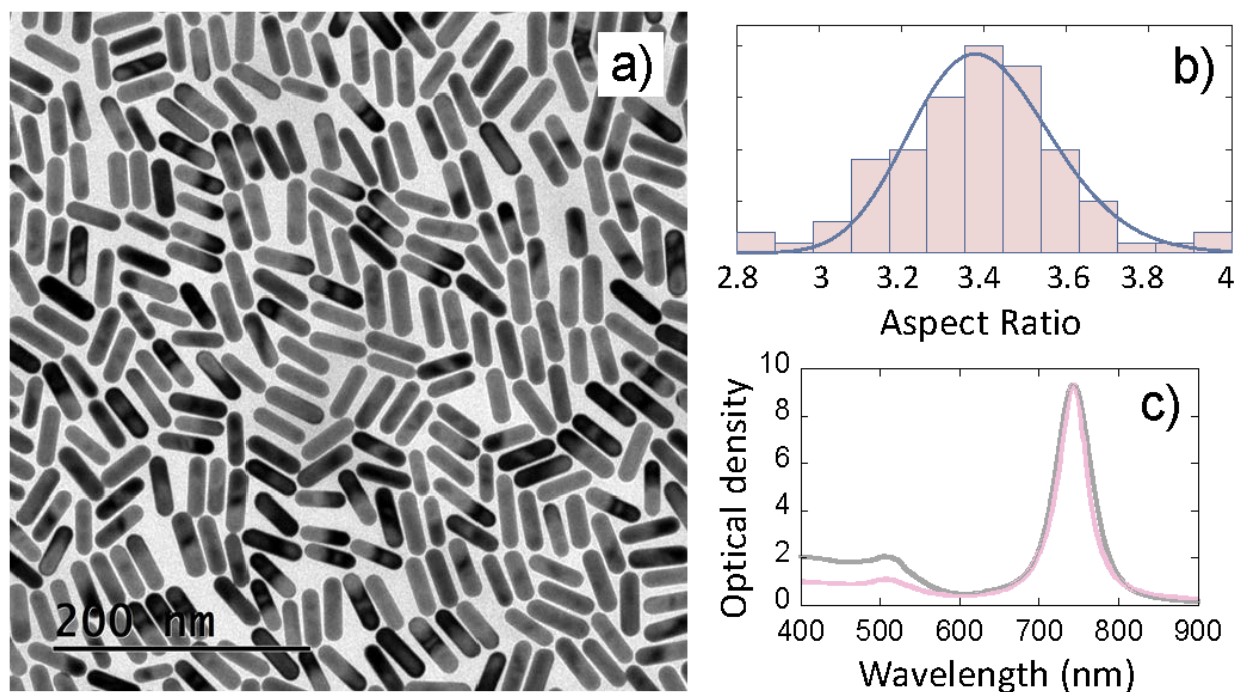
Figure 1. a) TEM images of the AuNRs used in the experiments. Particles resemble spherically capped cylinders with aspect ratio AR=3.4 and mean dimensions, l=45.7 nm and d=13.4 nm. b) Aspect ratio distribution determined from TEM images and associated density function (solid line). c) Experimental (pink) and calculated (grey) (Mie-Gans theory) optical extinction spectra.

The variation of the extinction spectra of aqueous AuNR dispersions with pressure is shown in Figures 2 and 3. It is worth noting that the use of monodisperse AuNR samples is crucial to get suitable optical spectra from dilute AuNR solutions in diamond anvil cells having light paths of about 70 μm. Usual AuNR solutions reported in the literature [16] have AR distributions with standard deviations typically around 0.4, which give rise to extinction spectra with LSPR bands having FWHM of 100 nm and extinction coefficients at the LSPR of 3000 nm². In contrast, our monodisperse AuNR solutions have FWHM values of 50 nm and the extinction coefficient is 8000 nm² (see Figure S2 in SI). This optical quality makes it possible to record suitable spectra from

dilute aqueous AuNR dispersions ([AuNR] = 3×10^{11} cm^{-3}) at high pressure, while minimizing effects due to aggregation and mutual interaction. We estimate that the signal-to-noise ratio enhancement using monodisperse AuNRs increases up to a factor of 5. In order to test the reproducibility of the measurements with this extremely sensitive AuNR system, we carried out three different pressure experiments, using three different samples taken from the same colloid. A pressure-induced redshift of the SPR is clearly observed in all three AuNR-water samples. The main observations were: 1) common and progressive LSPR redshifts, the pressure derivative of which decreases with pressure in a similar way to the variation of the water V_0/V ratio with pressure. 2) Abrupt LSPR jumps toward longer wavelengths at about 1.5 and 2.0 GPa, associated with the liquid-to-ice VI, and ice VI-to-ice VII phase transitions of water, respectively. The redshift pressure derivative changes with pressure and in each water phase. The largest SPR shift with pressure measured at low pressure ($P < 0.5$ GPa) in the liquid phase amounts to 22 nm/GPa (48 meV/GPa), which is a rather competitive figure for potential use of AuNRs as a low-pressure sensor in aqueous solutions. As a comparison, the pressure shift of ruby –the most widely used pressure sensor– is 0.36 nm/GPa [17]. 3) The LSPR band broadens with increasing pressure, after water solidification. In particular, LSPR broadening becomes more prominent in ice phase VII, where solidification-induced AuNR aggregation or stress are likely responsible for said broadening [4,18]. In addition, the variation of the optical density at the LSPR maximum, as a function of pressure, shows anomalies once hydrostaticity is lost (Figure 4). As expected from model simulations, we observed an increase of the maximum optical density with increasing pressure, due to the concomitant increase in medium refractive index, in the hydrostatic or quasi-hydrostatic pressure regimes. However, this trend does not hold after solvent hydrostaticity is lost, where the optical density at the LSPR maximum is found to decrease as pressure increases. Stress or

aggregation effects induced by non-hydrostaticity are likely responsible for this anomalous behavior of the optical density. It is worth noting that, whereas the solvent hydrostaticity loss has important consequences on the broadening and extinction damping of the LSPR peak, it only weakly affects the magnitude of LSPR pressure shifts. Correspondingly, no anomalous behavior of the LSPR variation is observed at pressures where the optical density decays.
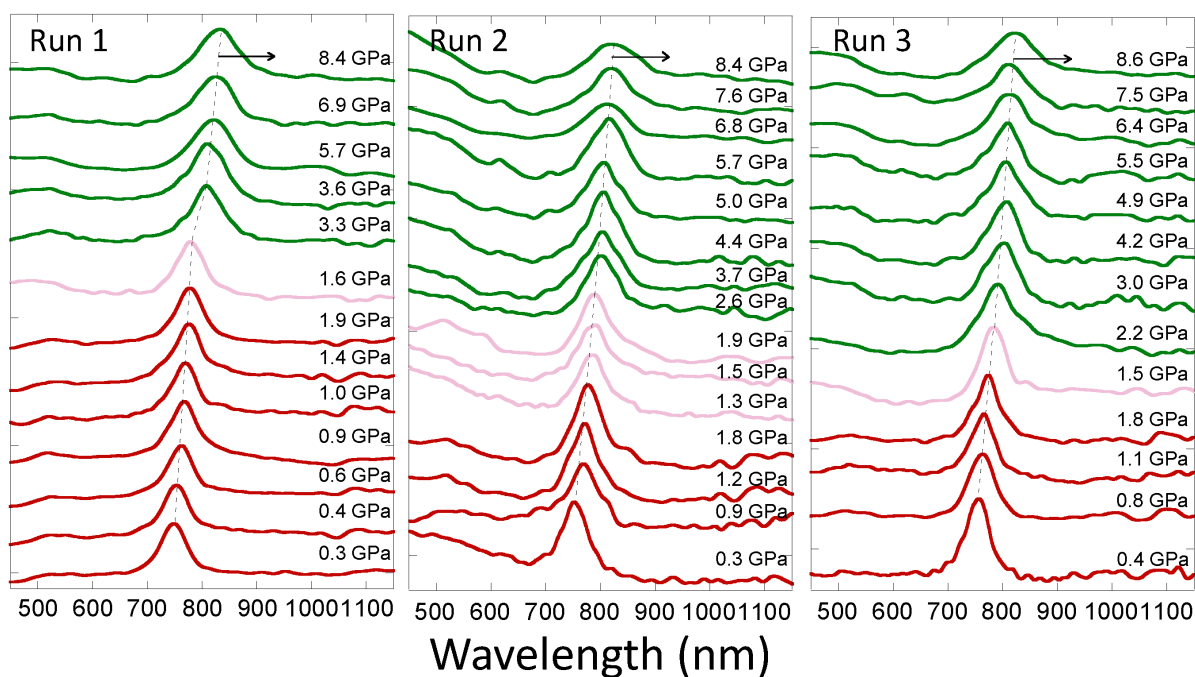

Figure 2. Extinction spectra of gold nanorods with AR=3.4, in aqueous solution, as a function of the pressure for three measurement runs. The spectra in red, pink and green refer to the liquid, ice VI and ice VII phases, respectively.
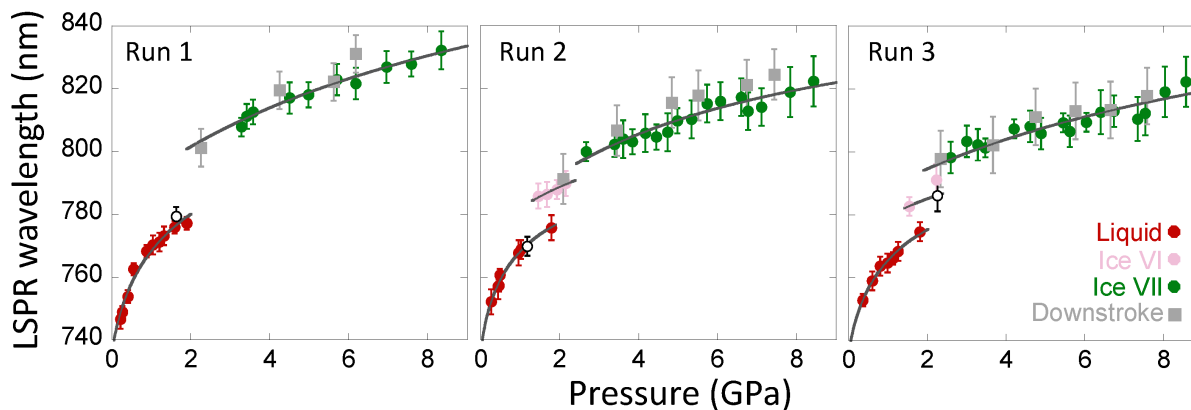
Figure 3. Pressure dependence of the LSPR band of gold nanorods with AR=3.4, in aqueous solution, for three measurement runs. The plots include experimental and calculated values of $\lambda_{LSPR}(P)$ using the Mie-Gans model. This model accounts for the LSPR behavior in the studied regime. Filled circles correspond to experimental data, and lines represent the calculated LSPRs. Empty circles (○) correspond to experimental points taken following pressure release attained after water-to-Ice VI transition at 1.8 GPa. This symbol at 2.0 GPa corresponds to phase coexistence at Ice VI–Ice VII phase transition. Calculation details are provided in the Discussion section.
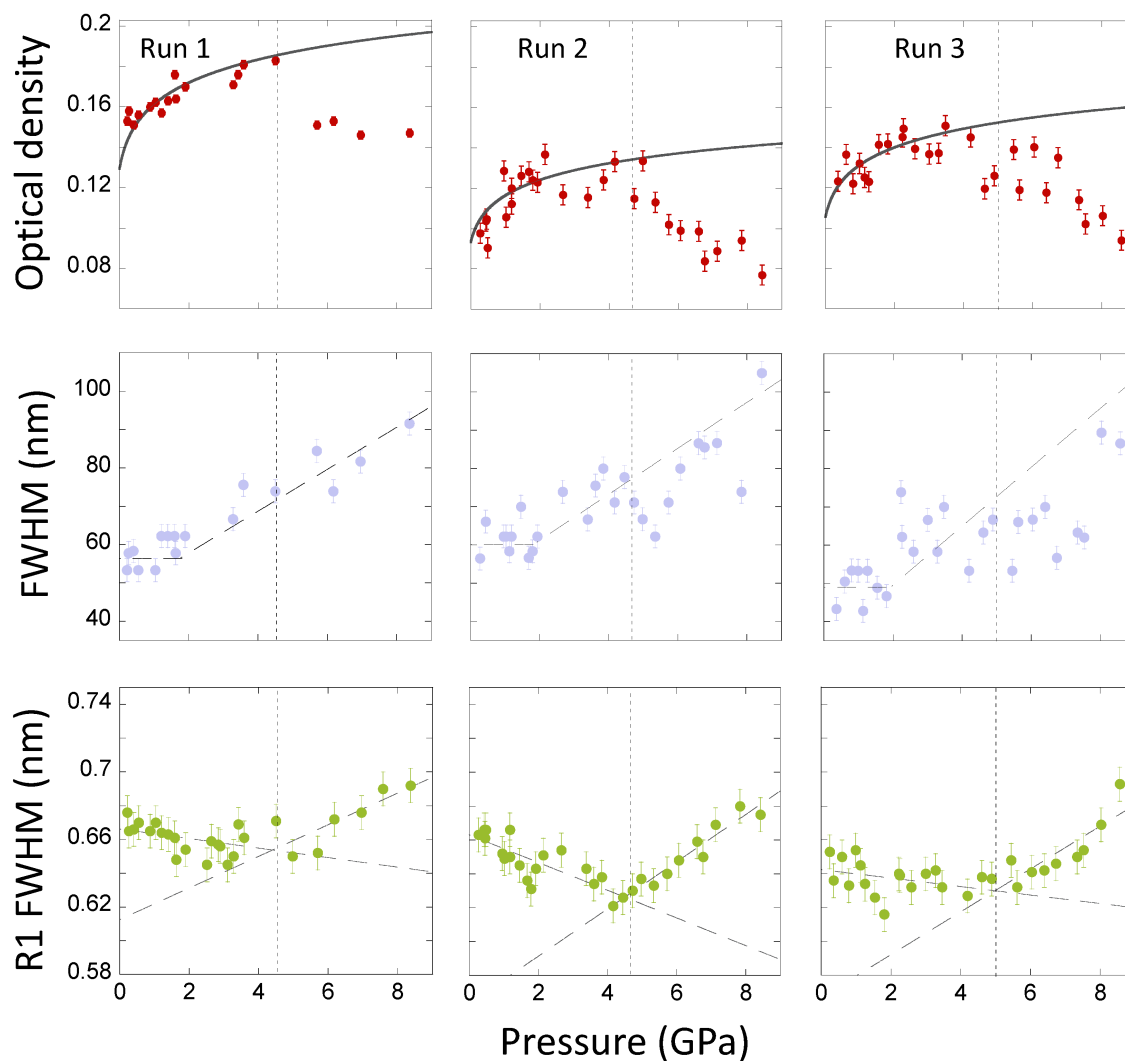
Figure 4. (Top row) Pressure dependence of the optical density at the LSPR band maximum. Solid line: calculated extinction cross-section from Mie-Gans theory. (Middle row) Pressure dependence of the FWHM of the LSPR band. Dashed lines are a visual guide, for both the liquid and solid states. (Bottom row) Hydrostatic pressure range of the solution. The vertical dotted line shows the hydrostaticity limit of the pressure transmitting medium (AuNR water solution). Note that after solidification (around 1.8 GPa) a quasi-hydrostatic regime is maintained.

DISCUSSION

We interpret the above results in terms of a modified Mie-Gans model [19], through which we can directly correlate the pressure-induced LSPR shift with the relative changes of AuNR volume and the solvent refractive index at each pressure, through the following equation:

$$\lambda_{LSPR} = \lambda_p(0)\sqrt{\frac{V}{V_0}}\sqrt{\varepsilon(0) + \frac{1-L}{L}\varepsilon_m} \qquad (1)$$

The variation with pressure of the optical density at the LSPR peak obeys:

$$I_{LSPR} = C\, V \varepsilon_m^{\frac{3}{2}}/\lambda_{LSPR} \qquad (2)$$

where $\lambda_p(0)$ and $\varepsilon(0)$ are the plasma wavelength at zero pressure and the short wavelength dielectric constant of gold, respectively. LSPR data of Fig. 3 have been analyzed using $\lambda_p(0) =$ 145.6 nm and (0) = 8.6. These values are closer to those reported for bulk gold by Olmon *et al*. [20] and Johnson and Christy [21] and provide the overall best fit. L is the nanorod depolarization or shape factor, $\varepsilon_m = n^2$ is the dielectric function of the non-absorbing medium, which also yields a refractive index, n, while C in Eq.2 is a renormalization constant. The change in particle volume can be well described by a first-order Murnaghan equation of state [22]

$$\frac{V}{V_0} = \left(\frac{PK_0'}{K_0} + 1\right)^{-1/K_0'} \qquad (3)$$

Here the bulk modulus $K = K_0 + K_0'P$ and $K_0' = \left(\frac{\delta K}{\delta P}\right)_{P=0}$. We employed a gold bulk modulus of $K_0 = 190$ GPa, with a fixed value of $K_0' = 6$ for the AuNR as determined by means of the reported

analysis of extinction spectra of gold nanocrystal colloids in ethanol-methanol mixtures over a range of hydrostatic pressures [4]. We found that the bulk modulus of gold for an AuNR of $K_0 = 190$ GPa is significantly higher than that for bulk gold metal, $K_0 = 167$ GPa [23]. This enhancement of the incompressibility for gold is a direct consequence of the nanoscale regime. From these data we could accurately determine the change in AuNR volume with pressure, to be incorporated in Eqs. (1) and (2). The parameter L was determined from analysis of TEM images (Figure 1). Given the quasi-isotropy of the solvent, we assumed that the AuNRs do not undergo reshaping under a hydrostatic load. A nanocrystal with cubic lattice, such as gold, should retain its shape upon volume reduction under high-pressure conditions. Hence, the analysis of pressure-induced LSPR shifts in AuNRs should reveal the pressure dependent solvent refractive index, over the explored pressure range. On the basis of the semi-empirical relationship between refractive index and mass density as $n \propto \rho$ [24], we describe the pressure dependence of the refractive index using a phenomenological Murnaghan-type equation:

$$n = n_0 \left(\frac{P\alpha}{\beta} + 1 \right)^{1/\alpha} \qquad (4)$$

where n_0 is the refractive index of water at ambient pressure, while α and β are empirical parameters. We determined these parameters by fitting the LSPR pressure shift to Eq. (1), using Eqs. (3) and (4) to describe the pressure dependence of gold electron density and solvent dielectric function as $\varepsilon_m = n^2$, respectively. The complete λ_{LSPR} (P) data were then fitted using Eq. (1), to obtain the pressure dependence of water refractive index, $n(P)$. Given the dispersion of $n(P)$ data in the literature [8–11, 25] we derived the water refractive index $n(P)$ directly from Eqs. 1 and 4. Interestingly, this procedure provides a semi-empirical analytical function for $n(P)$. In addition, compared to other techniques such as Brillouin scattering [8] or interferometric techniques [9-11],

this method has the advantage that the two main contributions to the LSPR shift are well known – the electron gas compression induces a blueshift while the refractive index of the medium induces a redshift – and can be easily decoupled, particularly for gold nanoparticles since the blueshift contribution from electron gas compression is much smaller – by about an order of magnitude – than the redshift contribution due to refractive index increase for compressed water. Knowledge of the blueshift generated by the increase of plasma frequency –electronic density $N(P)$ – for gold, allowed us to obtain the refractive index of water $n(P)$, since the contribution from $N(P)$ is not only smaller but also well known from the AuNR equation of state.

The suitability of Eq. (4) to describe the pressure dependence of the refractive index for water was evaluated against experimental $n(P)$ data reported by Polian *et al*. [8] from Brillouin scattering experiments using a density-based method, and by Dewaele *et al*. [9], Zha *et al*. [11], and Vedam and Limsuwan [10] from interferometric measurements (see Figures S3 and S4 in Supporting Information). The parameters β and α are only phenomenological parameters that should not be related to K_0 and K_0', respectively. We used the same β values for all phases in the fits –leaving two fitting parameters– in order to avoid parameter uncertainty and to allow comparison of the $n(P)$ values obtained by different experimental methods. We plotted in Figure 5 the $n(P)$ data obtained in this work, along with other results reported elsewhere [8–11]. We obtained very similar $n(P)$ values to those found for the liquid and ice VI phases by Polian *et al*. [8], Dewaele *et al*. [9], and Vedam and Limsuwan [10]. In the ice VII phase we observed better agreement with the results from refs. [9,11], especially in the high-pressure region, but with a good overall description of the data. Moreover, the $n(P)$ data extrapolated with our model (Eq. (4)) for pressures above 9 GPa are in excellent agreement with the experimental data reported by Zha *et al*. [11]. It is worth pointing

out that, here, we report analytical expressions describing $n(P)$ data for different phases of water: liquid, ice VI and ice VII, the corresponding parameters being collected in Table 1.

Table 1. Fitting parameters to the Murnaghan-type equation for each investigated water phase. The pressure range of applicability is also included. Errors correspond to the standard deviations derived from the fit of three runs for each phase.

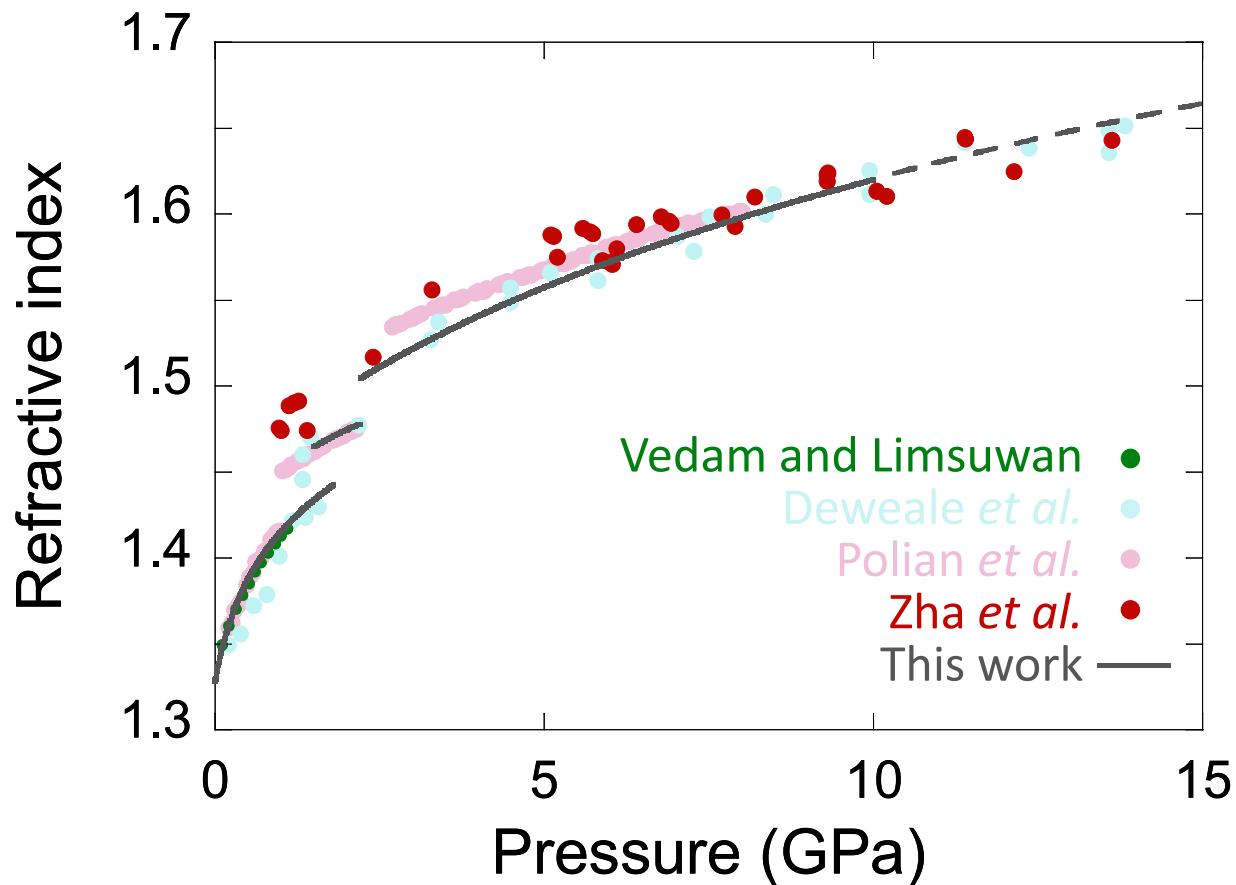|	Liquid	Ice VI	Ice VII
n_0	1.33 ± 0.01	1.40 ± 0.01	1.43 ± 0.03
α	26 ± 3	34 ± 3	13.7 ± 0.4
β	6 (fixed)	14 (fixed)	30 (fixed)
Pressure range (GPa)	$0 - 1.8$	$1.5 - 2.2$	$2.2 - 9$

Figure 5. Pressure dependence of water refractive index. Filled circles correspond to experimental data: (green) Vedam and Limsuwan [10], (blue) Dewaele *et al*. [9], (pink) Polian *et al*. [8], and (red) Zha *et al*. [11]. The later points were extracted from reported data by Zha *et al*. [11] and Pan *et al*. [26]. The solid lines represent experimental refractive index values obtained in this work, analyzed using Eq. 4. The dashed line is an extrapolation of our model outside the studied pressure range.

CONCLUSIONS

We have shown that the behavior of aqueous dispersions of gold nanorods under high pressure can be measured by optical spectroscopy using diamond anvil cells, and the observed effects are properly analyzed through changes induced in the LSPR of the gold nanorods. We demonstrate

that pressure-induced LSPR shifts provide information on the pressure dependence of the water refractive index. The method validity has been confirmed by comparing our $n(P)$ data for water to those obtained by other techniques. In particular, the surface plasmon spectroscopy-based $n(P)$ data are very similar to those obtained by combining Brillouin spectroscopy and sound velocity measurements under high-pressure conditions. Interestingly, the LSPR pressure shifts of aqueous AuNR dispersions are well described by a modified Mie-Gans model, in agreement with previous findings for AuNR dispersions in alcohol [4]. We also show that the analysis of the two main competing mechanisms responsible for LSPR –the compression of conduction electrons in the metal causes a blueshift while an increase in solvent density under pressure leads to a redshift– enables us to decouple both effects, thereby providing a direct approach to extract the variation of the refractive index of water $n(P)$ from the LSPR pressure shift across the three investigated water phases: liquid, ice VI and ice VII. Furthermore, we have demonstrated that the experimental $n(P)$ data can be accurately described by means of a semi-empirical, first-order Murnaghan-type equation, thus providing an analytical equation for the pressure-dependence of the water refractive index from 0 to 9 GPa. Our $n(P)$ data were validated against values determined by other techniques and reported elsewhere [8–11]. Indeed, extrapolation of our equation beyond the investigated pressure range provided excellent agreement with the available experimental data in the 9-15 GPa range. Besides, water exhibits a wide pressure range of quasi-hydrostaticity after its first solidification from liquid to ice VI, as we demonstrate by comparing pressure-induced peak/line broadening of the LSPR peak and ruby luminescence R lines, with FWHM that are highly sensitive to nonhydrostatic solvent stress. Nevertheless, such non-hydrostatic effects do not significantly affect the LSPR pressure shifts, as their variations with pressure show no measurable anomaly, in contrast to the optical density and FWHM of the LSPR bands.

A notable general conclusion of this work is the suitability of plasmonics for obtaining structural information on solvents as a function of pressure. The nanoparticles provide a chemically inert, high-pressure spectroscopy probe. We also stress that such plasmon based analysis benefits from the use of metal colloids with high monodispersity and therefore narrow plasmon bands.

EXPERIMENTAL PROCEDURES

Synthesis

Materials. Hydrogen tetrachloroaurate trihydrate ($HAuCl_4 \cdot 3H_2O$, 99.9%), hexadecyltrimethylammonium bromide (CTAB, 98%), silver nitrate ($AgNO_3$, ≥99.9%), 5-bromosalicylic acid (BrSal, 90%), L-ascorbic acid (≥99%), sodium borohydride ($NaBH_4$, 99%) and were used as received from Sigma-Aldrich. Nanopure water (resistivity 18.2 MΩ·cm at 25 °C) was used in all experiments.

Single-crystal gold nanorods with an average length of 45.7 nm and diameter of 13.4 nm and aspect ratio of 3.4 were synthesized. Firstly, standard AuNRs with LSPR band centered at 780 nm were synthesized via a seeded growth method with minor modifications [27]. Then, the aspect ratio dispersity of the synthesized AuNRs was reduced via femtosecond pulsed laser treatment according to a previously published procedure [7].

Seeds. The seeds were prepared by the standard CTAB/$NaBH_4$ procedure: 25 μL of a 0.05 M $HAuCl_4$ solution was added to 4.7 mL of a 0.1 M CTAB solution; 300 μL of a freshly prepared 0.01 M $NaBH_4$ solution was then injected under vigorous stirring. Excess borohydride was consumed by ageing the seed solution for 30 min at room temperature prior to use.

Gold nanorods with LSPR at 780 nm. In a typical synthesis, 45 mg of 5-bromosalicylic acid was added to 50 mL of 0.05 M CTAB and the mixture was mildly stirred for 15 min until complete dissolution. Then, 480 μL of 0.01 M AgNO$_3$, 500 μL of a 0.05 M HAuCl$_4$ and 200 μL of 0.1 M ascorbic acid solution were added to the mixture. After 2 h at 25 °C (or once the bromosalicylic acid has completely reduced Au (III) to Au (I), i.e., monitored by the reduction in the absorbance of the Au(III) CTAB complex at 390 nm), 50 μL of a 0.1 M ascorbic acid and 160 μL of the seed solution were added under vigorous stirring. After 2h, the resulting gold nanorods display LSPR maxima ranging from 820 to 890 nm. Fine tailoring of the LSPR to 780 nm was achieved via overgrowth of the synthesized gold nanorods. To afford controlled tuning of the LSPR the optimum amount of ascorbic acid needed was found experimentally by overgrowing small aliquots of the prepared nanorods with increasing volumes of the ascorbic acid solution: from 0.4 to 1 μL per mL. The mixture was left undisturbed at room temperature for at least 4 h. Then, the particles were washed three times for 40 min (8000 rpm, 30 °C) using 1 mM CTAB for redispersion.

Femtosecond pulse laser reshaping: Laser pulses (50 fs) were generated by an amplified Ti-Sapphire laser system (Spectra Physics), centered at 804 nm and operating at a repetition rate of 1 kHz. A TOPAS Prime automated optical parametric amplifier (OPA) was employed to generate laser pulses centered at 750 nm. The temporal profile of the pulses was diagnosed by second harmonic autocorrelation, whereas fluence control was performed by a variable attenuator wheel. The irradiation experiment was carried out using quartz cuvettes with an optical path of 5 cm (20 mL chamber volume, 200–2500 nm spectral range). The volume of the AuNRs suspension was fixed to 20 mL. The concentration of gold nanorods was maintained constant using a fixed value of the absorbance at 400 nm in a 1 cm optical path cuvette as a reference: 0.18. During the irradiation experiment, all the samples were stirred at a speed of 300 rpm using a magnetic bar.

The AuNRs (suspended in 1 mM CTAB aqueous solution) were irradiated using a fluence of 3.2 J/m2 for 3 hours.

TEM images were obtained in a JEOL JEM-2100 transmission electron microscope operating at an acceleration voltage of 200 kV. All samples were centrifuged prior to blotting on carbon-coated 400 square mesh copper grids.

High-pressure measurements

High-pressure experiments were carried out in a Böhler-Almax diamond anvil cell (DAC). Inconel 625 gaskets (200-μm thick) were preindented at 60-70 μm. Holes with 150 μm in diameter were perforated with a BETSA motorized electrical discharge machine as hydrostatic chambers. The DAC was loaded with aqueous AuNR colloids and ruby microspheres (10-20 μm diameter) as pressure probes [17]. The solutions themselves served as the pressure-transmitting media. The hydrostaticity of the pressure transmitting media was monitored through the ruby R-line broadening, the linewidth of which is known to slightly decrease with the pressure in the hydrostatic range.

Optical extinction spectra under high-pressure conditions at room temperature were recorded on a home-built fiberoptic based microscope, equipped with two Cassegrain 20× reflecting objectives mounted on two independent x-y-z translational stages for the microfocus beam, the objective lens and a third independent x-y translation stage for the DAC holder. Optical extinction data and images were obtained simultaneously with the same device [28]. Spectra in the UV-VIS and NIR range were recorded with 2 spectrometers, an Ocean Optics USB 2000 and a NIRQUEST 512, employing Si- and InGaAs-CCD detectors, respectively. The I and I0 intensities were measured in two separate experiments with the same DAC by loading it first with the nanoparticle colloid (I),

and then with the corresponding solvent (I0), covering the same pressure range. Three independent experiments were performed for the investigated dispersion to confirm that the results were reproducible and consistent. The hydrostatic pressure range and liquid-solid pressure transition of the AuNR solutions were determined from the pressure dependence of the FWHM of the ruby R-line emissions (see Figure 4).

ASSOCIATED CONTENT

Supporting Information contains detailed information on the following items. 1) Comparison between measured and simulated extinction spectra of a AuNR aqueous dispersion ([AuNR] = 3×10^{11} cm^{-3}). 2) Effects of polydispersity of AuNRs on the extinction spectra around the LSPR. 3) Murnaghan-type equation plots describing the refractive-index $n(P)$ of water as a function of pressure as measured by Brillouin spectroscopy and density data by Polian *et al*. 4) Murnaghan-type equation plots describing the refractive-index $n(P)$ of water as a function of pressure as determined by interferometric techniques by Dewaele *et al*.

AUTHOR INFORMATION

Corresponding Author

* Fernando Rodríguez. E-mail address: rodriguf@unican.es

Author Contributions

The manuscript was written through contributions from all authors. All authors have approved the final version of the manuscript.

ABBREVIATIONS

(AR), aspect ratio. (DAC), diamond anvil cell. (FWHM), full width at half maximum. (AuNR), gold nanorod. (LSPR), longitudinal surface plasmon resonance. (SI) supporting information. (SP), surface plasmon. (SPR), surface plasmon resonance.

REFERENCES

(1) El-Sayed, M. A. Small Is Different: Shape-, Size-, and Composition-Dependent Properties of Some Colloidal Semiconductor Nanocrystals. *Acc. Chem. Res.* **2004**, 37, 326-333.

(2) Pérez-Juste, J.; Pastoriza-Santos, I.; Liz-Marzán, J.M.; Mulvaney, P. Gold Nanorods: Synthesis, Characterization and Applications. *Coord. Chem. Rev.* **2005**, 249, 1870-1901.

(3) Nie, S.; Xing, Y.; Kim, G. J.; Simons, J. W. Nanotechnology Applications in Cancer. *Annu. Rev. Biomed. Eng.* **2007**, 9, 257-288.

(4) Martín-Sánchez, C.; Barreda-Argüeso, J. A.; Seibt, S.; Mulvaney, P.; Rodríguez, F. Effects of Hydrostatic Pressure on the Surface Plasmon Resonance of Gold Nanocrystals. *ACS Nano*, **2019**, 13, 498-504.

(5) Bao, Y.; Zhao, B.; Tang, X.; Hou, D.; Cao, J.; Tang, S.; Liu, J.; Wang, F.; Cui, T.; Tuning Surface Plasmon Resonance by the Plastic Deformation of Au Nanoparticles within a Diamond Anvil Cell. *Appl. Phys. Lett*. **2015**, 107, 201909.

(6) Christofilos, D.; Assimopoulos, S.; Del Fatti, N.; Voisin, C.; Vallèe, F.; Kourouklis. G. A.; Ves, S.; High-pressure Study of the Surface Plasmon Resonance in Ag Nanopartilces. *High Pressure Res*. **2003**, 23, 23-27.

(7) González-Rubio, G.; Díaz-Núñez, P.; Rivera, A.; Prada, A.; Tardajos, G.; González-Izquierdo, J.; Bañares, L.; Lombart, P.; Macdoweel, L. G.; Alcolea-Palafox, M.; Liz-Marzán, L. M.; Peña-Rodríguez, O.; Guerrero-Martínez, A. Femtosecond laser reshaping yields gold nanorods with ultranarrow suface plasmon resonances. *Science*, **2017**, 358, 640-644.

(8) Polian, A.; Grimsditch, M. Brillouin scattering from H_2O: Liquid, ice VI, and ice VII. *Phys. Rev. B*, **1983**, 27, 6409-6412.

(9) Dewaele, A.; Eggert, H. J.; Loubeyre, P.; Le Toullec, R. Measurement of refractive index and equation of state in dense He, H_2, H2O, and Ne under high pressure in a diamond anvil cell. *Phys. Rev. B*, **2003**, 67, 0094112.

(10) Vedam, K.; Limsuwan, P. Piezo- and elasto-optic properties of liquids under high pressure. II. Refractive index vs density. *J. Chem. Phys*. **1978**, 69, 4772-4778.

(11) Zha, C.; Hemley, R. J.; Gramsch, S. A.; Mao, H.; Bassett. W. A. Optical study of H_2O ice to 120 GPa: Dielectric function, molecular polarizability, and equation of state. *J. Chem. Phys.* **2007**, 126, 074506.

(12) Wu, J.; Xiang, D.; Gordon, R. Characterizing gold nanorods in aqueous solution by acoustic vibrations probed with four-wave mixing. *Opt. Express*, **2016**, 24, 12458-12465.

(13) Prescott, S.W.; Mulvaney, P. Gold Nanorod Extinction Spectra. *J. Appl. Phys.* **2006**, 99, 123504.

(14) Pecharromán, C.; Pérez-Juste, J.; Mata-Osoro, G.; Liz-Marzán, L. M.; Mulvaney, P. Redshift of surface plasmon modes of small gold rods due to their atomic roughness and end-cap geometry. *Phys. Rev. B*, **2008**, 77, 035418.

(15) Yu, R.; Liz-Marzán, L. M.; García de Abajo, F. J. Universal analytical modeling of plasmonic nanoparticles, *Chem. Soc. Rev.*, **2017**, 46, 6710-6724.

(16) Link, S.; Mohamed, M. B.; El-Sayed, M. A. Simulation of the Optical Absorption Spectra of Gold Nanorods as a Function of Their Aspect Ratio and the Effect of the Medium Dielectric Constant, *J. Phys. Chem. B*, **1999**, 103, 3073-3077.

(17) Syassen, K. Ruby Under Pressure. *High Pressure Res.* **2008**, 28, 75-126.

(18) Umar A.; Choi, S. M. Aggregation Behavior of Oppositely Charged Gold Nanorods in Aqueous Solution, *J. Phys. Chem. C*, **2013**, 117, 11738-11743.

(19) Gans, R. Über die Form Ultramikroskopischer Goldteilchen. *Ann. Phys.* **1912**, 342, 881-900.

(20) Olmon, R. L.; Slovick, B.; Johnson, T. W.; Shelton, D.; Oh, S.; Boreman, G. D.; Raschke, M. B. Optical Dielectric Function of Gold, *Phys. Rev. B*, **2012**, 86, 235147.

(21) Johnson, P. B; Christy, R. W. Optical Constants of Noble Metals. *Phys. Rev. B*, **1972**, 6, 4370-4379.

(22) Grady, D. Equation of state for solids. *AIP Conference Proceedings*, **2012**, 1426, 800-803.

(23) Heinz, D. L.; Jeanloz, R. The Equation of State of the Gold Calibration Standard. *J. Appl. Phys*. **1984**, 55, 885-893.

(24) Liu, Y.; Daum, P. H. Relationship of refractive index to mass density and selfconsistency of mixing rules for multicomponent mixtures like ambient aerosols. *J. Aerosol Sci.*, **2007**, 39, 974-986.

(25) Huang, Y.; Zhang, X.; Ma, Z.; Zhou, Y.; Zheng, W.; Zhou, J.; Sun. C. Q. Hydrogen-bond relaxation dynamics: Resolving mysteries of water ice. *Coord. Chem. Rev*, **2015**, 285, 109-165.

(26) Pan, D.; Wan, Q.; Galli, G. The refractive index and electronic gap of water and ice increase with increasing pressure. *Nat. Commun*. **2014**, 5, 3919.

(27) Scarabelli, L.; Grzelczak, M.; Liz-Marzán, L. M. Tuning Gold Nanorod Synthesis through Prereduction with Salicylic Acid. *Chem. Mater*. **2013**, 25, 4232-4238.

(28) Barreda-Argüeso J. A.; F. Rodríguez. F. Patent No. PCT/es2014/000049.
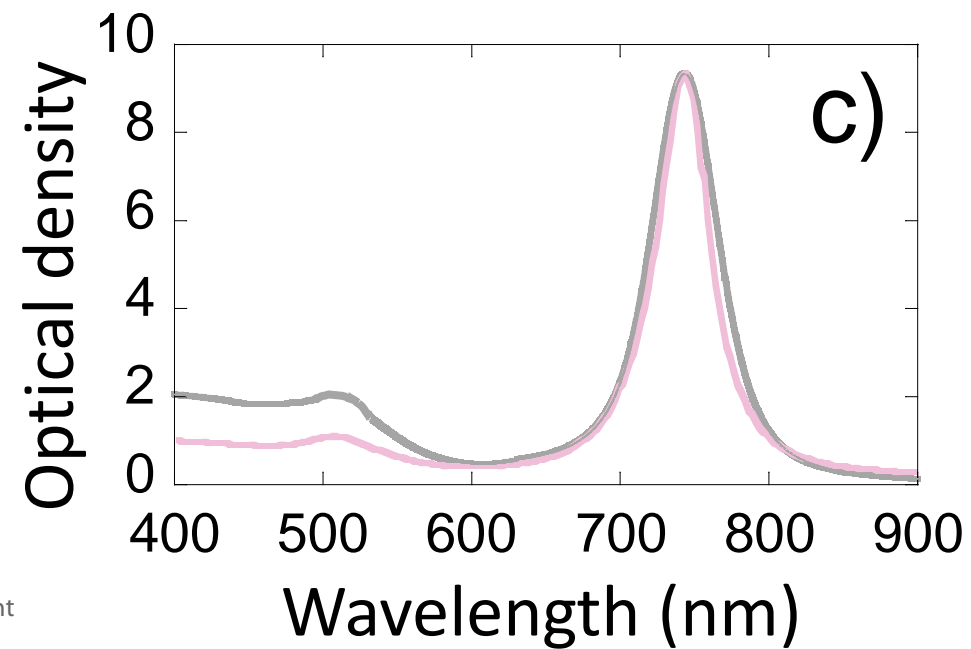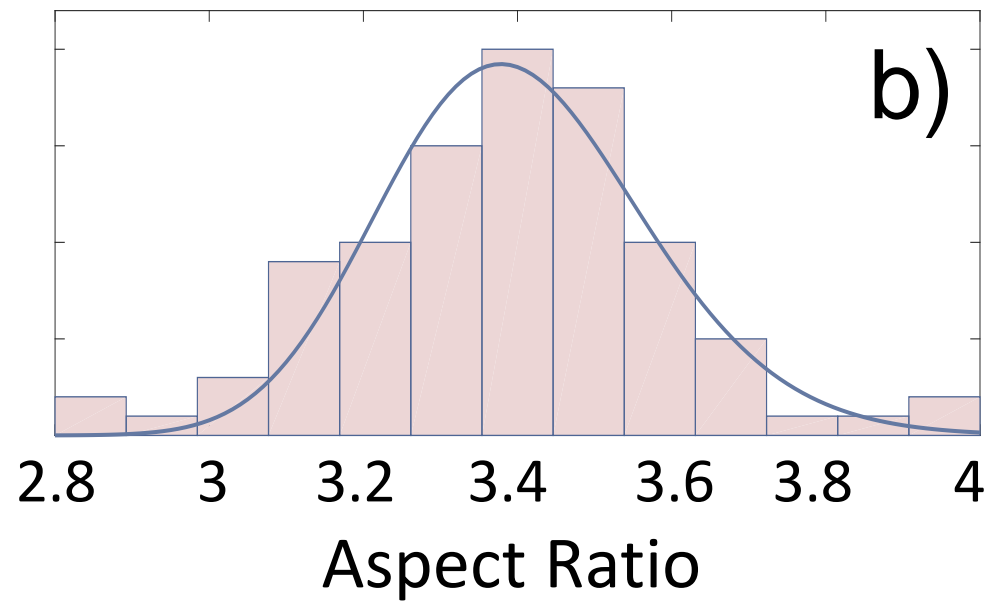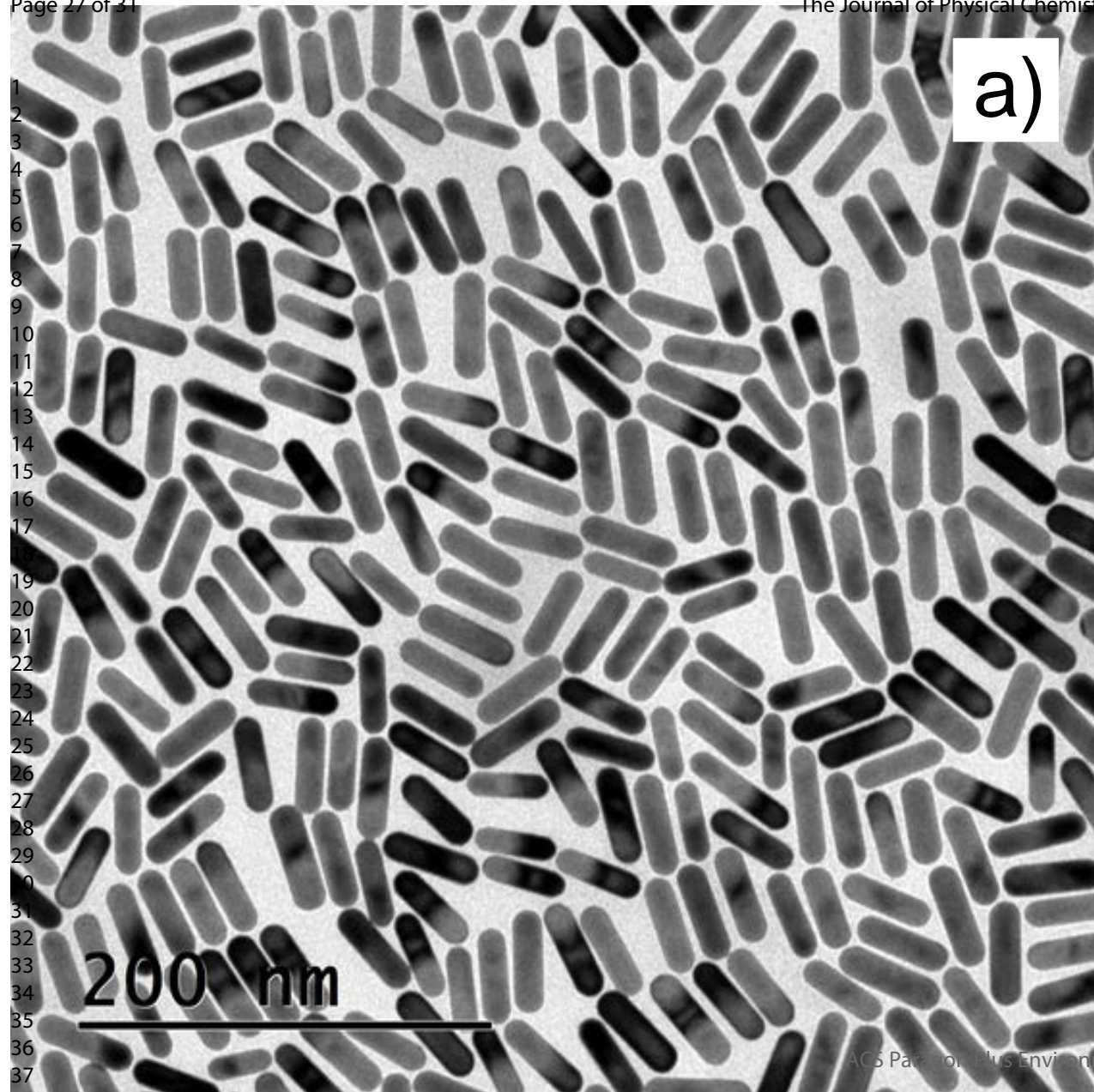
(29) Olinger B.; Halleck. P. M. Compression and bonding of ice VII and an empirical linear expression for the isothermal compression of solids. *J. Chem. Phys.*, **1975**, 62, 94-99.
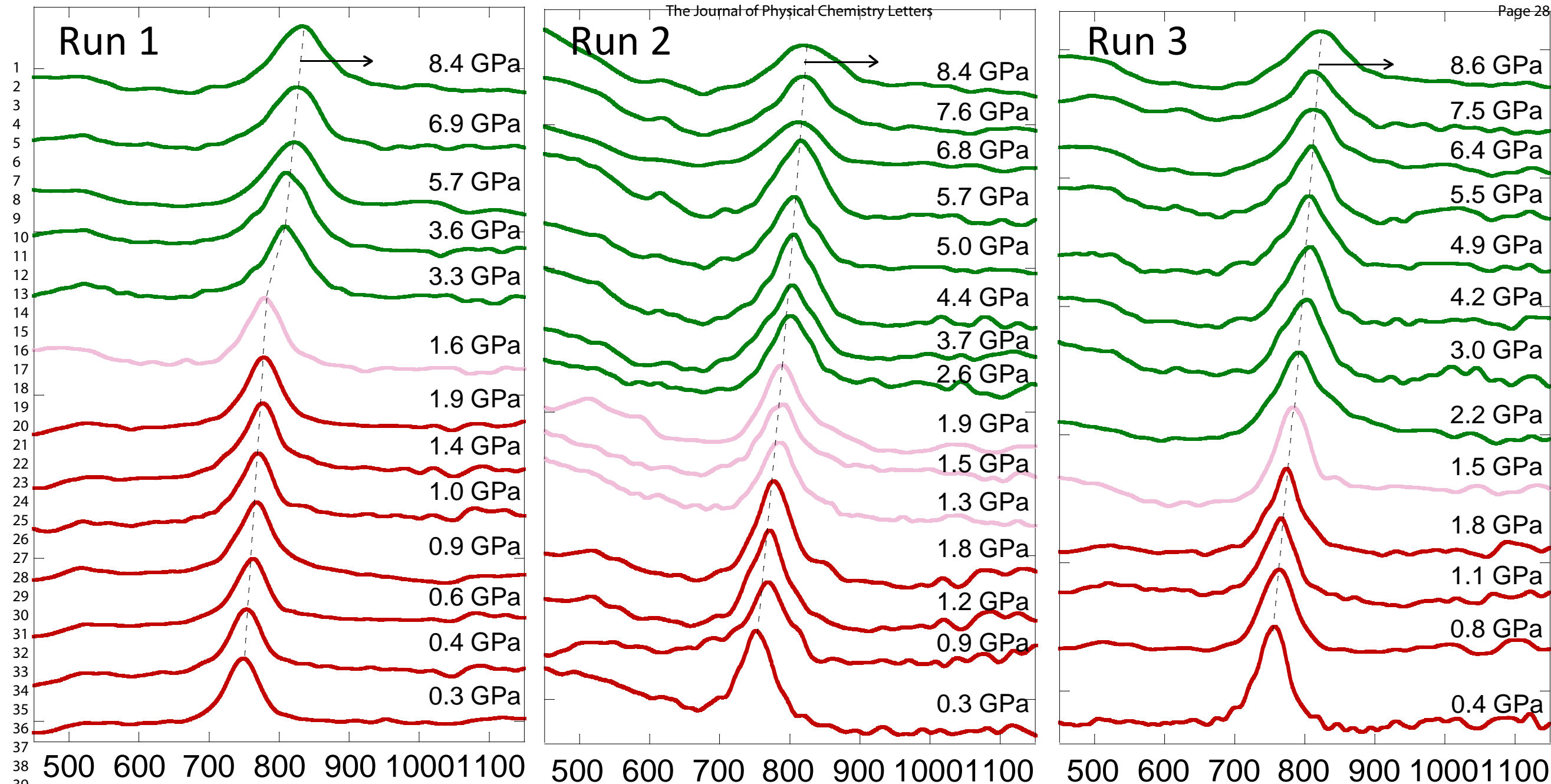
1
2
3
4
5
6
7
8
9
10
11
12
13
14
15
16
17
18
19
20
21
22
23
24
25
26
27
28
29
30
31
32
33
34
35
36
37
38
39
40
41
42
43
44
45
46
47
48
49
50
51
52
53
54
55
56
57
58
59
60

BRIEFS. The high-pressure effects on the surface plasmon resonances (SPR) of aqueous dispersions of monodisperse gold nanorods have been measured. Pressure-induced shifts of the ultranarrow longitudinal SPR enable determination of pressure phase transitions and the pressure dependence of the refractive index along the liquid, ice VI and ice VII phases of water.
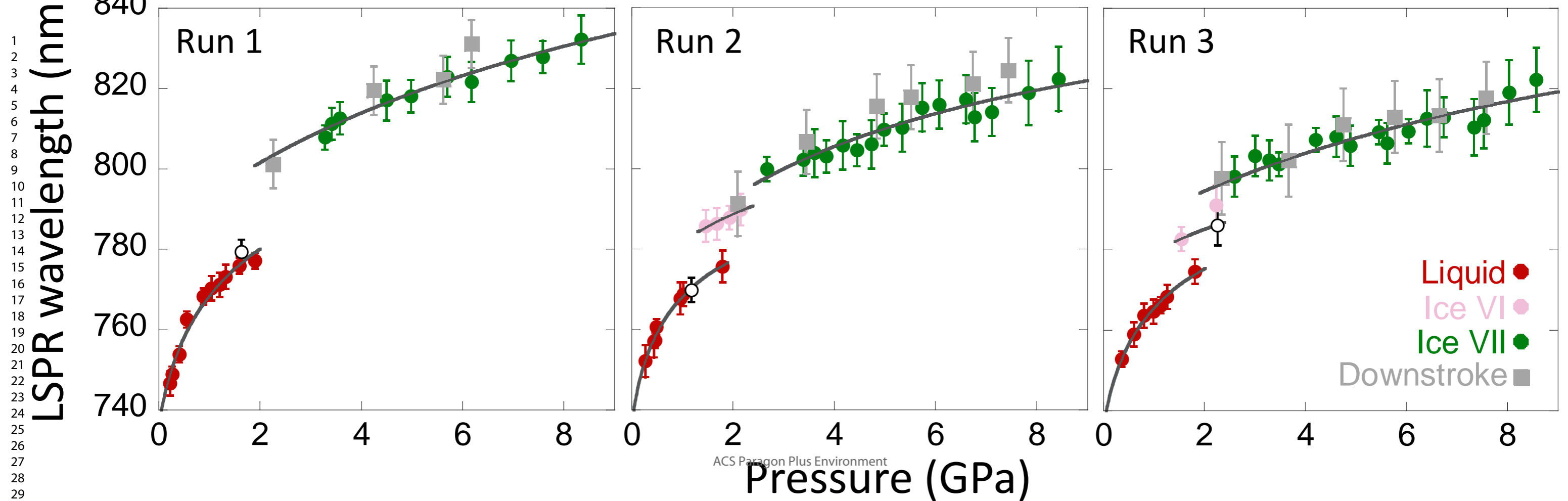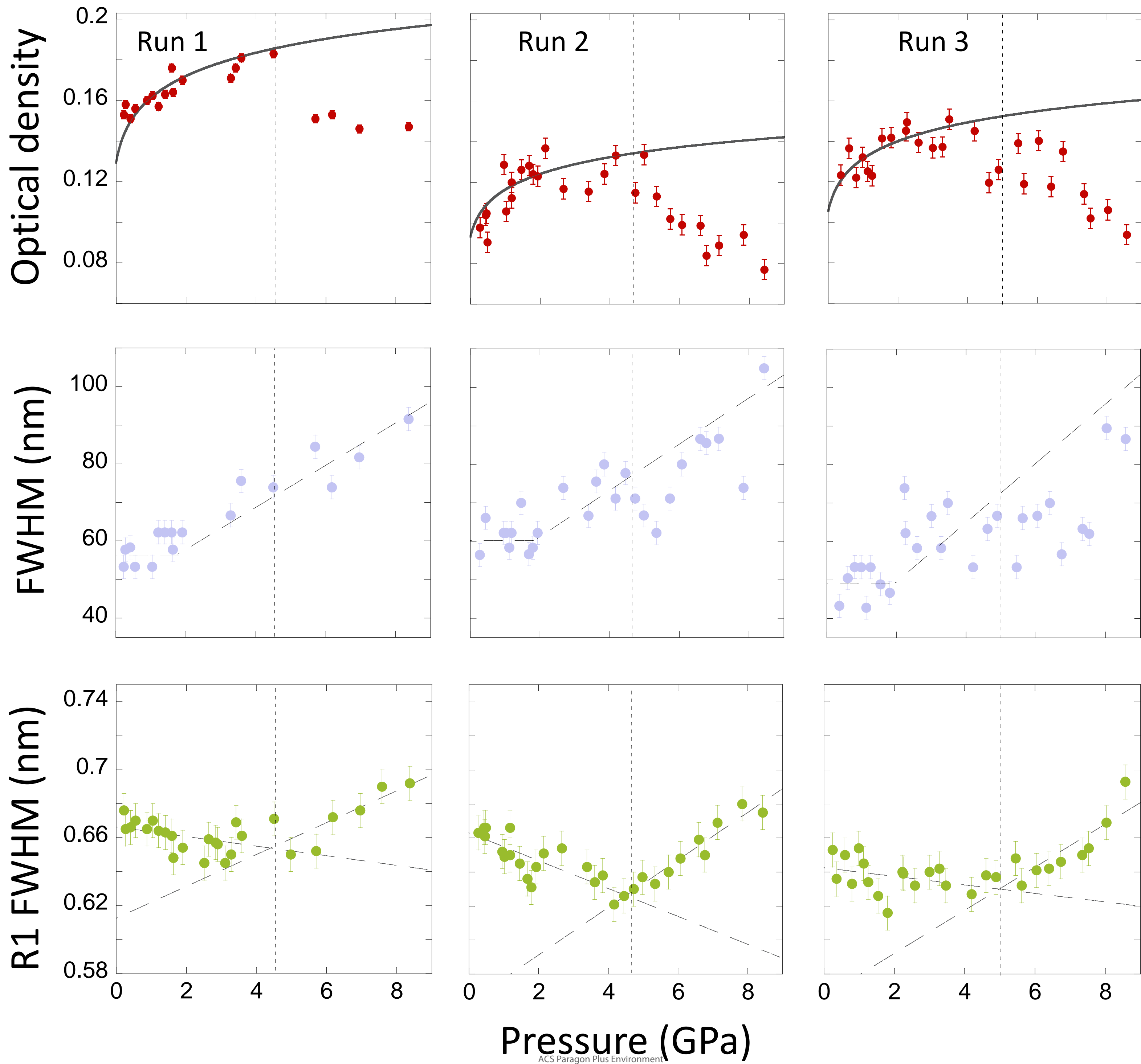

SYNOPSIS TOC.

1
2
3
4
5
6
7
8
9
10
11
12
13
14
15
16
17
18
19
20
21
22
23
24
25
26
27
28
29
30
31
32
33
34
35
36
37
38
39
40
41
42
43
44
45
46
47
48
49
50
51
52
53
54
55
56
57
58
59
60